Accepted Manuscript
Version of record at: https://doi.org/10.1002/adom.202100783

Controlling Microring Resonator Extinction Ratio via Metal-Halide Perovskite Nonlinearity

Feifan Wang, Lianfeng Zhao, Yahui Xiao, Tiantian Li, Yixiu Wang, Anishkumar Soman, Hwaseob Lee, Thomas Kananen, Xiaoyong Hu, Barry P. Rand,* and Tingyi Gu*

F. Wang, Y. Xiao, T. Li, Y. Wang, A. Soman, H. Lee, T. Kananen, T. Gu
Electrical and Computer Engineering
University of Delaware
Newark, DE 19711, USA
E-mail: tingyigu@udel.edu
F. Wang, X. Hu
State Key Laboratory for Mesoscopic Physics & Department of Physics
Collaborative Innovation Center of Quantum Matter & Frontiers Science
Center for Nano-Optoelectronics
Beijing Academy of Quantum Information Sciences
Peking University
Beijing 100871, P. R. China
L. Zhao, B. P. Rand
Department of Electrical Engineering
Princeton University
Princeton, NJ 08544, USA
E-mail: brand@princeton.edu

Abstract
The exceptionally high optical nonlinearities, wide bandgap, and homogeneity in solution-processed metal-halide perovskite media are utilized as optical nonlinear elements on a silicon photonic platform for low-power-active components, such as all-optical switches, modulators, and lasers. With room temperature back-end-of-line compatible processing, a hybrid metal-halide perovskite ($CH_3NH_3PbI_3$) microring resonator (MRR) structure is fabricated on a foundry-processed low-loss silicon photonic platform. With in-plane excitation near the light intensity of 110 W m^{-2}, strong two-photon absorption and free-carrier absorption saturation are observed. With 10^3 field enhancements by MRRs, the photorefractive effect in the metal-halide perovskite reduces linear absorption, represented by 10^2 improvement of the MRR's intrinsic quality factor and 20 dB enhancement of the extinction ratio.

Introduction

Metal-halide perovskites constitute an emerging optoelectronic material with exceptionally high efficiency in solar cells and light-emitting devices.[1-5] Beyond these applications, metal-halide perovskites also exhibit interesting nonlinear phenomena,[6] such as tunable optical nonlinearities,[7] and ultrafast and broadband responses.[8, 9] Their large multiphoton absorption rate[10-13] leads to unique free-carrier gain for higher-energy photons.[14] Their exceptional nonlinear properties lead to applications in passive Q-switched lasers,[15-17] upconversion light emitters and lasers,[18, 19] and optical limiters[20] to low photon energy detectors.[14, 21]

The third-order nonlinear coefficients, including the Kerr coefficient and two-photon absorption (TPA) rate, are the fundamental characteristic parameters. Z-scan is the most convenient technique to obtain those coefficients; however, the result is subjected to distortions from other concurrent nonlinear processes, such as free-carrier and thermal dispersions, and photorefractive effect. Furthermore, reported values obtained by the Z-scan technique are not consistent.[22-24] The mismatch might be attributed to the metal-halide perovskites' air sensitivity, where the oxidation-related defect states or introduction of water alters optical properties. Given silicon's weak nonlinear coefficient, the mature silicon photonic platform serves as a passive and robust platform for characterizing the nonlinear coefficient of hybrid integrated materials, such as ultrafast electro-optic modulators[25] and detectors,[26] TPA-induced optical bistabilities,[27] and mid-gap defect state absorptions.[28] The characterized nonlinear coefficient of the hybrid waveguide can be used for designing active silicon photonic components for low-power all-optical switching and modulation.

In this work, we present the optical nonlinearities of hybrid $CH_3NH_3PbI_3$–silicon waveguides and microring resonators (MRRs) for low-power optical communications. The photon propagation pathway is defined by the low-loss silicon photonic waveguides,[29] with evanescent coupling to the solution-integrated $CH_3NH_3PbI_3$ layer. The low mid-gap states' density and smooth surface of the solution-processed $CH_3NH_3PbI_3$ ensure low propagation loss of the hybrid waveguide for nonlinear optics studies,[30-32] while environmental impacts are minimized via encapsulation. Under continuous wave (CW) excitation, the two-photon-absorption-generated free-carrier absorption (FCA) is characterized by a hybrid waveguide structure and compared to control samples of air-cladding waveguides. Under 6 fJ energy pulse excitation through input waveguide, the strong absorption modulation leads to 10 dB enhancement of extinction ratio (ER) in a hybrid resonator. The reduced material absorption improves the MRR's quality factor (Q) from 10^4 to 10^5. The results are verified by a set of MRRs defined on the same chiplet and explained by coupled-mode theory (CMT) fittings.

Accepted Manuscript
Version of record at: https://doi.org/10.1002/adom.202100783

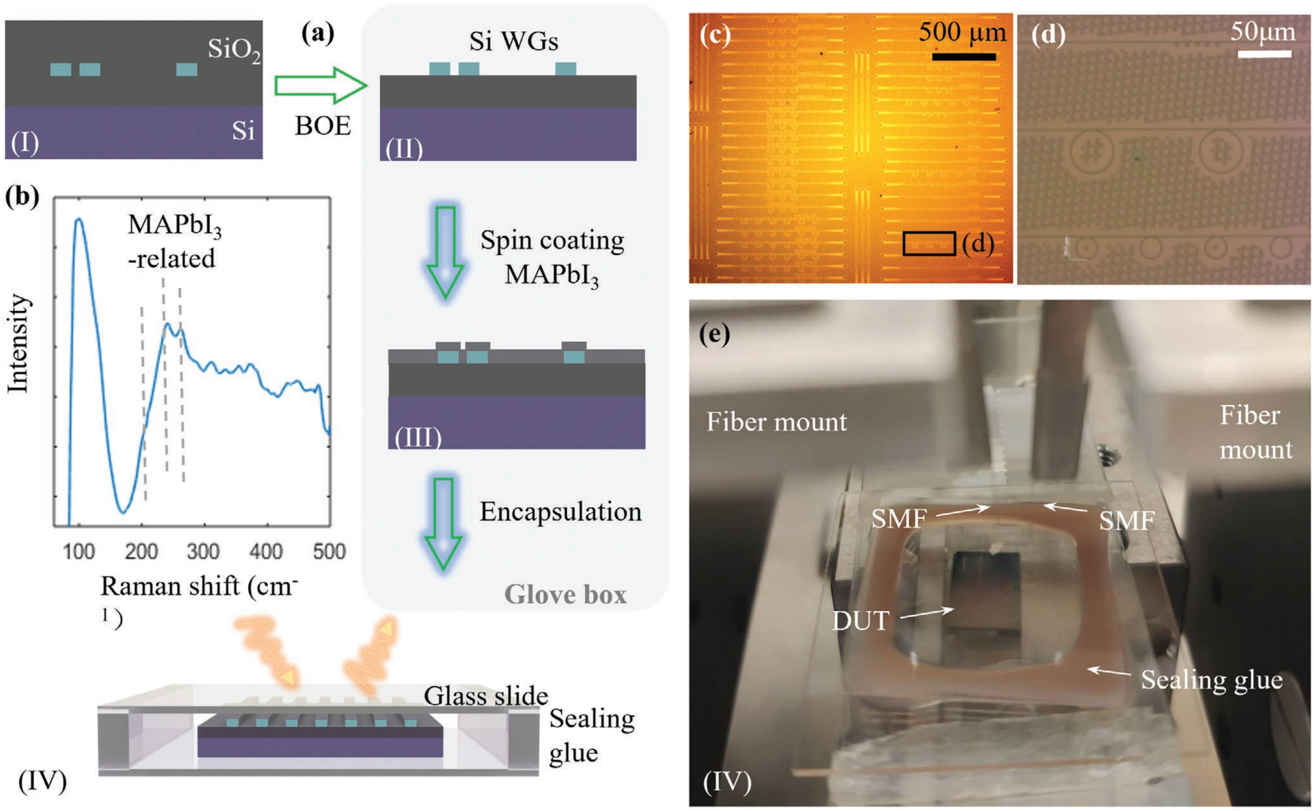

Figure 1. Device preparation and characterization. a) Schematics of the hybrid device fabrication. The hybrid integration processes (II–IV) are carried out in a nitrogen-filled glovebox. BOE: buffered oxide etchant. b) Micro-Raman spectra of the packaged device in panel (a). c) Optical image of the silicon photonic devices with d) waveguide-coupled MRR arrays. e) Measurement of the packaged device (step IV in panel (a)). SMF: single-mode fiber. DUT: device under test.

2. Device Fabrication

The fabrication process of the $MAPbI_3$-covered (MA: methylammonium or $CH_3NH_3^+$) sample is shown in **Figure 1**a. The foundry-processed low-loss photonic waveguides and resonators are defined on a silicon-on-insulator (SOI) substrate with an oxide cladding layer. The thickness of the top cladding layer, the silicon layer, and the oxide isolation layer are 5.4 µm, 220 nm, and 2 µm, respectively. The oxide cladding layer is first removed by dipping in buffered oxide etchant. A 200 nm thick $MAPbI_3$ film is spin-coated on the device layer, and the hybrid device is encapsulated to minimize any oxygen-related degradation during measurement. For the encapsulation, the sample is placed on a thick glass slide and covered with a thin glass slide, then sealed with ultraviolet epoxy between the two glass slides to make an airtight glass case. The spin-coating and encapsulation processes are performed in a nitrogen-filled glovebox. The packaged device is then taken out of the glovebox for optical characterization. The micro-Raman spectra of the packaged device show characteristic Raman peaks of $MAPbI_3$ at 204.5, 241.4, and 262.7 cm^{-1} (Figure 1b).[33,34]

The silicon photonic substrates include MRR arrays (Figure 1c,d), with six resonators coupled onto the same bus waveguide. The radii of the MMRs vary between 10 and 20 µm. The device is then mounted on a fiber probe stage (Figure 1e). The infrared light is coupled in and out of the devices from the grating couplers defined on the silicon device layer (Experimental Section). The hybrid solution integration increases the propagation loss from <2.5 to ≈20 dB cm^{-1}. The propagation loss of 2.5 dB cm^{-1} in the monolithic device is comparable to the value reported by the nanomanufacturing foundry,[35] indicating a clean wet-etching process.

3. Nonlinear Coefficient of the Hybrid Waveguide

We first characterize the nonlinear absorption in a hybrid single-mode waveguide. The incident photon energy (0.8 eV) is below the bandgap of $MAPbI_3$,[36] and thus the nonlinear absorption in the single-mode waveguide is dominated by TPA and related FCA

$$\alpha(I) = \alpha_0 + \overline{\beta_2} I + \overline{\beta_2}\sigma'\tau I^2 \quad (1)$$

where α_0 is the linear loss coefficient of the waveguide and I is the ratio between input power and effective mode area A_{eff} (≈1.2 × 10^{-13} m^2 for TPA and 9.7 × 10^{-14} m^2 for FCA) of the hybrid waveguide (Section S1, Supporting Information).[37,38] The TPA coefficients of silicon are 5×10^{-12} and 3.6×10^{-6} m W^{-1} for $MAPbI_3$.[39,40] The resulting field-balanced effective TPA

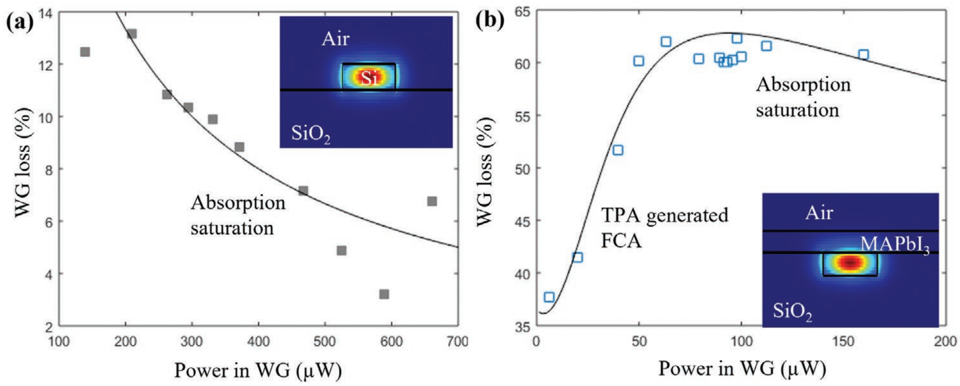

Figure 2. Power-dependent total propagation loss in 0.8 mm long a) air-clad silicon waveguide and b) hybrid MAPbI$_3$–Si waveguide. Squares: experimental data. Solid black curves: models. Insets: cross-sectional optical mode profiles at 1550 nm.

$\overline{\beta_2}$ is calculated to be 1.9 × 10^{-8} m W^{-1} ($\chi^{(3)} \approx 10^{-9}$ esu) (Section S2, Supporting Information). The third term in Equation (1) represents the free-carrier absorption in the hybrid waveguide. σ' is proportional to the absorption cross section of free carriers. τ is the effective free-carrier lifetime. Under CW excitation, the free carrier absorption is usually orders of magnitude stronger than two-photon absorption.[41] Based on a first-order approximation, the power-dependent waveguide transmission can be expressed as

$$T = \frac{e^{-\alpha_0 L}}{\overline{\beta_2}\sigma'\tau I^2 L_{\mathrm{eff}} + 1} \tag{2}$$

where T is the transmission of the waveguide, α is the effective linear absorption coefficient, L = 800 μm is the length of the waveguide, and $L_{\mathrm{eff}} = \frac{1-\exp(-\alpha L)}{\alpha}$ is the effective length of the waveguide.[42] Another power-dependent factor is absorption saturation. The total absorption ($A = 1 - T$) can be divided into a part that can be saturated (e.g., linear as well as nonlinear absorption) and the rest (e.g., scattering). The total absorption $A' = AR/(1 + I/I_0) + A\ (1 - R)$, where I_0 is the saturation power intensity and R is the portion of the saturable absorption. In air-clad silicon waveguides, only absorption saturation is observed (gray solid squares in **Figure 2**a). By fitting the absorption saturation model into the experiment, I_0 is derived to be 0.1 MW cm^{-2} in both monolithic and hybrid waveguides, while R = 1 in the air-clad waveguide (WG) and R = 0.6 in the hybrid WG.The product of $\overline{\beta_2}\sigma'\tau$ is derived to be 8 × 10^{-15} m^3 W^{-2}. Ultrafast pulsed excitation provides a higher peak power and reduced free-carrier responses than CW excitation,[41] which are of paramount importance for studying parametric nonlinearities, such as four-wave mixing, parametric oscillation, and harmonic generations.

4. Photorefractive Effect in Microring Resonators

By reaching the upper limit of the input optical power, the field-enhancement effect[43–45] in an optical resonator provides access to the nonlinear response of the material response. Here, the hybrid MAPbI$_3$–Si MRRs are fabricated by following the procedures given in Figure 1a. The transmission spectra of a waveguide with multiple side-coupled MRRs can be expressed as $T = \prod T_i$. The transmission spectra of a waveguide coupled MRR ($T_i = T_{1,2,3}$) can be derived from the CMT[46,47]

$$T_i(\omega) = \left| 1 - \frac{\kappa_c 2}{-j(\omega-\omega_0)+\kappa_c 2+\kappa_{in} 2} \right|^2 \tag{3}$$

where ω_0 is the resonance angular frequency of the MRR, ω is that of the input laser, $\kappa_c^2 = 1/\tau_c$ is the photon coupling rate to the waveguide, and $\kappa_{in}^2 = 1/\tau_{in}$ is the intrinsic photon loss rate through scattering radiation and material absorption. Given the dominant material absorption in the device, κ_{in}^2 is proportional to the nonlinear propagation loss in the waveguide as described in Equation (1). The intrinsic, coupling, and total Qs are defined as $Q_{in} = \omega_0\tau_{in}$, $Q_c = \omega_0\tau_c$, and $Q_{total} = \omega_0\tau_{total}$, respectively. The total cavity lifetime depends on the coupling and intrinsic cavity lifetimes: $1/\tau_{total} = 1/\tau_c + 1/\tau_{in}$, where ω_0 is the resonance angular frequency of the MRR. The resonance frequency shift probes the real part of the refractive index change with high precision: $\Delta n = n_{\mathrm{eff}}(\Delta\omega_0/\omega_0)/\Gamma$, where n_{eff} is the effective index of the hybrid waveguide. The mode confinement factor in MAPbI$_3$, Γ, is derived to be ≈18% (inset of Figure 2b). More details of the calculation for Γ can be found in Section S1 (Supporting information).

By fitting the CMT model to the experimental data, the intensity enhancement factor is derived to be ≈10^3, which means that light intensity up to 0.15 W can be achieved in the MRR. The light intensity is three orders of magnitude higher in MRR than the WG as shown in Figure 2b. We observed a strong photorefractive effect at these light intensities, which means the incident light permanently changes complex refractive index in the material.[48] Suppressed material absorption (≈1/15) and refractive index change (≈3 × 10^{-4}) are observed (**Figure 3**). The reduced material absorption is characterized by the manifested Q_{in} in the resonators (Figure 3a,b). Three resonators with 20 μm radii (named as $R1$, $R2$, and $R3$, with resonance wavelengths of around 1538 nm) exhibit similar behavior. The coupling rate for the three MRRs is around 2 × 10^{10} s^{-1}. At low input power (P_1 = –15 dBm), the intrinsic photon loss is so high (>10^{11} s^{-1}) that the resonance dips are hard to distinguish (gray

Accepted Manuscript
Version of record at: https://doi.org/10.1002/adom.202100783

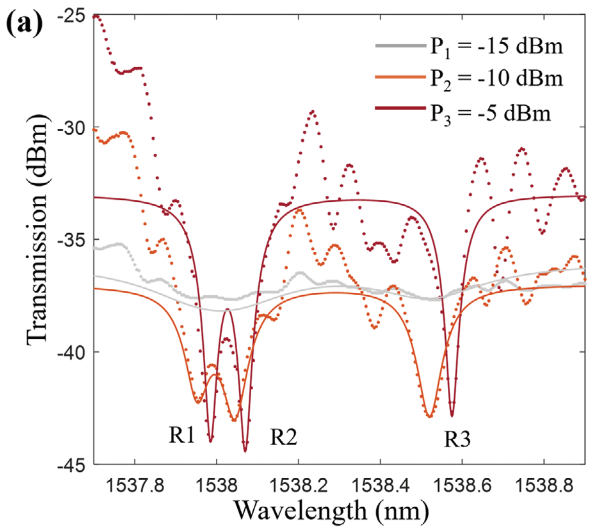

(b)

Q_{in}	P$_1$	P$_2$	P$_3$
R1	< 8k	52k	122k
R2	< 9k	53k	122k
R3	< 9k	56k	122k

(c)

	Q_{total}	$\Delta\lambda$
R1	36.0k	33 pm
R2	38.3k	25 pm
R3	39.5k	55 pm

Figure 3. Power-dependent transmission spectra of an MRR side-coupled to a waveguide. a) The input power level in the bus waveguide is −15 dBm (gray), −10 dBm (orange), and −5 dBm (red). The dots are experimental data, and the solid curves are from CMT fitting. b) Extracted intrinsic Q (Q_{in}) for the three MRRs ($R1$, $R2$, and $R3$) at the three input power levels in panel (a). c) Extracted total Q (Q_{total}) and resonance shift at P3.

dashed curve in Figure 3a). The loss rate is suppressed five times by increasing the input power to −10 dBm (orange dots), which leads to clear observation of the resonance transmission line shape. At −5 dBm input power, the ERs are measured to be around 10 dBm, and the Q_{in} increases from ≈10^4 to ≈10^5. Along with the suppressed material absorption, the change of the real part of the absorption is characterized by the resonance wavelength shifts ($\Delta\lambda$) (Figure 3c).

It is noted that the change of the line shape is due to a photorefractive effect rather than transient optical nonlinearities, because 1) those resonance line shapes are fully symmetric, and 2) the line shapes are repeatable when the input power is reduced to P_1. The suppressed material loss and enhanced Q_{in} are permanent in the MRRs. As the local light intensity is beyond the photorefractive threshold, the photorefractive dispersion is stronger than the transient optical nonlinear dispersions, such as TPA and FCA.[48] Given the field enhancement effect in the ring (10^3), the local light intensity reaches 0.1 GW cm^{-2}, with an input light intensity of 100 µW.

ER is a key performance factor for MRR-based optical filters, switches, and modulators. It is defined as the ratio between on-resonance transmission and off-resonance transmission of the MRR. To verify the observation of material nonlinearity enhanced ERs in the hybrid ring, we measured a set of MRRs with a radius of 10 µm, which are coupled to the same waveguide, and compared to correspondent sets of monolithic MRRs manufactured in the same multiproject wafer run (**Figure** 4). We observed the consistent behavior of power-dependent ERs. The ER of a monolithic silicon MRR is nearly constant at increasing power levels (gray curve in Figure 4). The ERs in the hybrid MRRs increase ≈10 dB at similar power levels. The results are consistent among the six MRRs under test. Given slightly different geometric design and fabrication, the unique nonlinear effect is repeatable among different devices.

5. Conclusion

In this work, we experimentally demonstrate integrated $MAPbI_3$–silicon photonic waveguides and resonators. In the hybrid WG, we observed stronger TPA and free-carrier absorption saturation at sub-milliwatt input power levels. With cavity field enhancement, the light intensity exceeds the photorefractive effect threshold in $MAPbI_3$, leading to significantly suppressed linear absorption. The reduced absorption is represented by manifested Q and ER in the hybrid MRR. The ER increases from 3 to 20 dB with femtojoule input optical energy

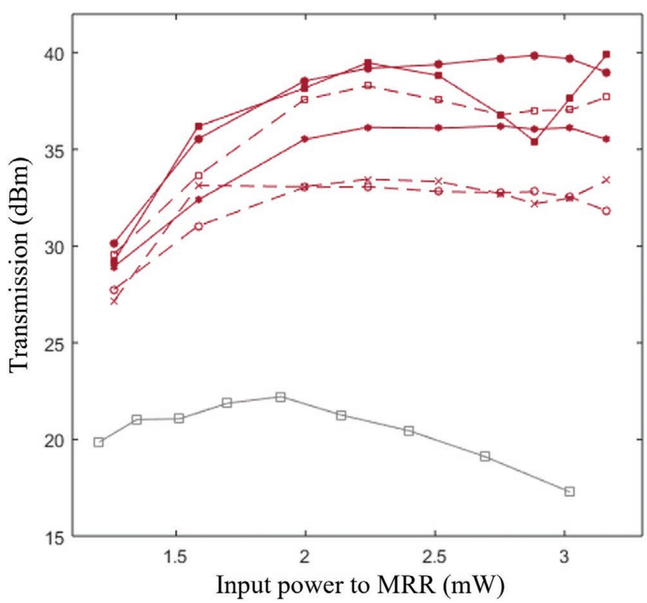

Figure 4. Experimentally measured extinction ratio in monolithic (gray) and hybrid (red) MRRs with 10 µm radius.

(0.11 mW input power). The results are repeatable among a set of MRRs with $Q_{total} \approx 10^4$.

6. Experimental Section

Sample Fabrication: Top oxide of the original sample from AIM photonics was removed with buffered oxide etching (BOE) 1:6 liquids. PbI_2 and MAI were dissolved in *N,N*-dimethylformamide anhydrous (Sigma–Aldrich, 99.8% anhydrous) to obtain a 1 M $MAPbI_3$ solution. The solution was dropped onto the sample, and a 200 nm thick $MAPbI_3$ film was deposited by spin coating at 6000 rpm. A solvent exchange step was performed after 3.5 s by dropping toluene on the spinning samples. Then, samples were annealed at 70 °C for 5 min. Finally, the sample was moved onto a thick glass slide and covered with a thin glass slide. The sample was sealed with ultraviolet epoxy between the two glass slides to avoid possible degradation in air.

Device Characterization: CW light generated from a tunable laser was sent onto chip through a polarization controller and single-mode fiber, and coupled onto the hybrid waveguide through a grating coupler. The tunable laser power fluctuation was less than ±0.01 (0.05) dB or less in 5 min (1 h). The output light was collected by a power meter.

Supporting Information

Supporting Information is available from the Wiley Online Library or from the author.

Acknowledgements

This work was supported by Army Research Office 75900ELYIP and Air Force Office of Scientific Research FA9550-18-1-0300. L.Z. and B.P.R. acknowledge Air Force Office of Scientific Research Award No. FA9550-18-1-0037.

Conflict of Interest

The authors declare no conflict of interest.

Data Availability Statement

The data that support the findings of this study are available from the corresponding author upon reasonable request.

Keywords

absorption saturation, microring resonator, perovskites, photorefraction, two-photon absorption

[1] X. Liu, W. Xu, S. Bai, Y. Jin, J. Wang, R. H. Friend, F. Gao, *Nat. Mater.* **2020**, *20*, 10.
[2] Y. Jia, R. A. Kerner, A. J. Grede, A. N. Brigeman, B. P. Rand, N. C. Giebink, *Nano Lett.* **2016**, *16*, 4624.
[3] Y. Wang, X. Li, X. Zhao, L. Xiao, H. Zeng, H. Sun, *Nano Lett.* **2016**, *16*, 448.
[4] F. O. Saouma, C. C. Stoumpos, J. Wong, M. G. Kanatzidis, J. I. Jang, *Nat. Commun.* **2017**, *8*, 742.
[5] L. Wu, K. Chen, W. Huang, Z. Lin, J. Zhao, X. Jiang, Y. Ge, F. Zhang, Q. Xiao, Z. Guo, Y. Xiang, *Adv. Opt. Mater.* **2018**, *6*, 1800400.
[6] W. Chen, F. Zhang, C. Wang, M. Jia, X. Zhao, Z. Liu, Y. Ge, Y. Zhang, H. Zhang, *Adv. Mater.* **2021**, *33*, 2004446.
[7] S. Liu, G. Chen, Y. Huang, S. Lin, Y. Zhang, M. He, W. Xiang, X. Liang, *J. Alloys Compd.* **2017**, *724*, 889.
[8] J. Li, C. Ren, X. Qiu, X. Lin, R. Chen, C. Yin, T. He, *Photonics Res.* **2018**, *6*, 554.
[9] K. N. Krishnakanth, S. Seth, A. Samanta, S. V. Rao, *Opt. Lett.* **2018**, *43*, 603.
[10] I. Suárez, M. Vallés-Pelarda, A. F. Gualdrón-Reyes, I. Mora-Seró, A. Ferrando, H. Michinel, J. R. Salgueiro, J. P. Martínez Pastor, *APL Mater.* **2019**, *7*, 041106.
[11] R. A. Ganeev, K. Srinivasa Rao, Z. Yu, W. Yu, C. Yao, Y. Fu, K. Zhang, C. Guo, *Opt. Mater. Express* **2018**, *8*, 1472.
[12] A. Ferrando, J. P. Martínez Pastor, I. Suárez, *J. Phys. Chem. Lett.* **2018**, *9*, 5612.
[13] F. Zhou, X. Ran, D. Fan, S. Lu, W. Ji, *Adv. Opt. Mater.* **2021**, *10*, 2100292.
[14] G. Walters, B. R. Sutherland, S. Hoogland, D. Shi, R. Comin, D. P. Sellan, O. M. Bakr, E. H. Sargent, *ACS Nano* **2015**, *9*, 9340.
[15] W. Shen, J. Chen, J. Wu, X. Li, H. Zeng, *ACS Photonics* **2021**, *8*, 113.
[16] J. Li, H. Dong, B. Xu, S. Zhang, Z. Cai, J. Wang, L. Zhang, *Photonics Res.* **2017**, *5*, 457.
[17] R. Zhang, J. Fan, X. Zhang, H. Yu, H. Zhang, Y. Mai, T. Xu, *ACS Photonics* **2016**, *3*, 371.
[18] Z. Hu, Z. Liu, Y. Bian, D. Liu, X. Tang, W. Hu, Z. Zang, M. Zhou, L. Sun, J. Tang, Y. Li, J. Du, Y. Leng, *Adv. Opt. Mater.* **2017**, *5*, 1700419.
[19] M. T. Hill, M. C. Gather, *Nat. Photonics* **2014**, *8*, 908.
[20] M. Jin, X. Liang, H. Zhang, J. Liu, G. Shao, W. Xiang, Y. Song, *J. Eur. Ceram. Soc.* **2020**, *40*, 4140.
[21] F. Zhou, I. Abdelwahab, K. Leng, K. P. Loh, W. Ji, *Adv. Mater.* **2019**, *31*, 1904155.
[22] J. Xu, X. Li, J. Xiong, C. Yuan, S. Semin, T. Rasing, X. Bu, *Adv. Mater.* **2020**, *32*, 1806736.
[23] F. O. Saouma, D. Y. Park, S. H. Kim, M. S. Jeong, J. I. Jang, *Chem. Mater.* **2017**, *29*, 6876.
[24] T. C. Wei, S. Mokkapati, T. Y. Li, C. H. Lin, G. R. Lin, C. Jagadish, J. H. He, *Adv. Funct. Mater.* **2018**, *28*, 1707175.
[25] J. Leuthold, C. Koos, W. Freude, *Nat. Photonics* **2010**, *4*, 535.
[26] C. Liu, J. Guo, L. Yu, J. Li, M. Zhang, H. Li, Y. Shi, D. Dai, *Light: Sci. Appl.* **2021**, *10*, 123.
[27] T. Gu, J. F. McMillan, N. W. Petrone, A. van der Zande, J. C. Hone, M. Yu, G. Q. Lo, D. L. Kwong, C. W. Wong, *Opt. Commun.* **2014**, *314*, 23.
[28] T. Gu, M. Yu, D. L. Kwong, C. W. Wong, *Opt. Express* **2014**, *22*, 18412.
[29] F. Wang, L. Zhao, H. Lee, Y. Xiao, T. Li, Y. Wang, A. Soman, T. Kananen, X. Hu, B. P. Rand, T. Gu, *Conf. Lasers Electro-Opt., Conference on Lasers and Electro-Optics (CLEO_QELS 2021)*, OSA Technical Digest, Optical Society of America, San Jose, CA **2021**, unpublished paper JW1A.47.
[30] J. Endres, D. A. Egger, M. Kulbak, R. A. Kerner, L. Zhao, S. H. Silver, G. Hodes, B. P. Rand, D. Cahen, L. Kronik, A. Kahn, *J. Phys. Chem. Lett.* **2016**, *7*, 2722.
[31] Z. Xiao, R. A. Kerner, L. Zhao, N. L. Tran, K. M. Lee, T.-W. Koh, G. D. Scholes, B. P. Rand, *Nat. Photonics* **2017**, *11*, 108.
[32] C. Xie, C.-K. Liu, H.-L. Loi, F. Yan, *Adv. Funct. Mater.* **2020**, *30*, 1903907.

[33] R. Gottesman, L. Gouda, B. S. Kalanoor, E. Haltzi, S. Tirosh, E. Rosh-Hodesh, Y. Tischler, A. Zaban, C. Quarti, E. Mosconi, F. De Angelis, *J. Phys. Chem. Lett.* **2015**, *6*, 2332.
[34] P. Pistor, R. Alejandro Ruiz, A. Cabot, V. Izquierdo-Roca, *Sci. Rep.* **2016**, *6*, 35973.
[35] https://www.aimphotonics.com/process-design-kit.
[36] W. Ahmad, J. Khan, G. Niu, J. Tang, *Sol. RRL* **2017**, *1*, 1700048.
[37] C. Koos, P. Vorreau, T. Vallaitis, P. Dumon, W. Bogaerts, R. Baets, B. Esembeson, I. Biaggio, T. Michinobu, F. Diederich, W. Freude, J. Leuthold, *Nat. Photonics* **2009**, *3*, 216.
[38] V. S. Afshar, T. M. Monro, C. M. de Sterke, *Opt. Express* **2013**, *21*, 18558.
[39] T. Gu, N. Petrone, A. van der Zande, J. Hone, M. Yu, G.-Q. Lo, D.-L. Kwong, C. W. Wong, *Opt. Commun.* **2014**, *314*, 23.
[40] J. Yi, L. Miao, J. Li, W. Hu, C. Zhao, S. Wen, *Opt. Mater. Express* **2017**, *7*, 3894.
[41] X. Yang, C. W. Wong, *Opt. Express* **2007**, *15*, 4763.
[42] J. Xing, J. Zhao, X. Wen, K. Wang, P. Lu, Q. Xiong, *Adv. Opt. Mater.* **2017**, *5*, 1601045.
[43] W. Bogaerts, P. De Heyn, T. Van Vaerenbergh, K. De Vos, S. K. Selvaraja, T. Claes, P. Dumon, P. Bienstman, D. Van Thourhout, R. Baets, *Laser Photonics Rev.* **2012**, *6*, 47.
[44] J. Heebner, R. Grover, T. Ibrahim, *Optical Microresonators: Theory, Fabrication and Applications*, 1st ed., Springer, London **2008**.
[45] Y. H. Wen, O. Kuzucu, M. Fridman, A. L. Gaeta, L.-W. Luo, M. Lipson, *Phys. Rev. Lett.* **2012**, *108*, 223907.
[46] B. E. Little, S. T. Chu, H. A. Haus, J. A. F. J. Foresi, J.-P. Laine, *J. Lightwave Technol.* **1997**, *15*, 998.
[47] H. Lee, T. Kananen, A. Soman, T. Gu, *IEEE Photonics Technol. Lett.* **2019**, *31*, 813.
[48] R. W. Boyd, *Nonlinear Optics*, Academic Press, San Diego, CA **2020**.